

# Knowledge Discovery in Nanophotonics Using Geometric Deep Learning

Yashar Kiarashinejad, Mohammadreza Zandehshahvar, Sajjad Abdollahramezani, Omid Hemmatyar, Reza Pourabolghasem, and Ali Adibi\*

Herein, a new approach for using the intelligence aspects of artificial intelligence for knowledge discovery rather than device optimization in electromagnetic (EM) nanostructures is presented. This approach uses training data obtained through full-wave EM simulations of a series of nanostructures to train geometric deep learning algorithms to assess the range of feasible responses as well as the feasibility of a desired response from a class of EM nanostructures. To facilitate the knowledge discovery, this approach combines the dimensionality reduction technique with convex-hull and one-class support-vector-machine (SVM) algorithms to find the range of the feasible responses in the latent response space of the EM nanostructure. More importantly, the one-class SVM algorithm can be trained to provide the degree of feasibility of a response from a given nanostructure. This important information can be used to modify the initial structure to an alternative one that can enable an initially unfeasible response. To show the applicability of this approach, it is applied to two important classes of binary metasurfaces (MSs), formed by an array of plasmonic nanostructures, and periodic MSs formed by an array of dielectric nanopillars. These theoretical and experimental results confirm the unique features of this approach for knowledge discovery in EM nanostructures.

## 1. Introduction

Photonic nanostructures have been of great recent interest due to their unique capabilities to manipulate the properties of electromagnetic (EM) waves beyond what conventional bulk materials can do. Due to their constituent nanoscale features, which can spectrally, spatially, or temporally control the optical state of EM waves with subwavelength resolution, nanophotonic devices offer all the functionalities realized by conventional bulky optical devices in much smaller footprints.<sup>[1–7]</sup> Combined with the


advances in nanofabrication technologies, these nanostructures have been used to demonstrate devices with enormous potential for groundbreaking technologies such as computing,<sup>[8–11]</sup> imaging,<sup>[12]</sup> energy harvesting,<sup>[13,14]</sup> and electronics to name a few.

Design of photonic devices in the nano-scale regime outperforming the bulky optical components has been a long-lasting challenge in state-of-the-art applications. Accordingly, devising a comprehensive model to understand and explain the fundamental physics of light–matter interaction in these nanostructures is a substantial step toward the realization of novel nanophotonic devices. To this end, existing modeling methods can be categorized into two main groups: single- and multi-objective approaches. Single-objective approaches either rely on exhaustive design parameter sweeps using a brute-force EM solver (e.g., based on the finite element method [FEM])<sup>[15]</sup> or evolve from an initial guess to a final result through evolutionary methods

(e.g., genetic algorithm).<sup>[16]</sup> Although the former requires extensive computation, the latter highly depends on the initial guess and in most cases converges to a local optimum. Parameterized adjoint optimization can also be used to design high-performance metasurfaces (MSs) which are easy to use; however, they are computationally expensive.<sup>[17,18]</sup> All of these single-objective approaches are computationally demanding and fail when the input–output relation is complex, or the number of desired features for a nanostructure grows. In contrast, multi-objective methods<sup>[19,20]</sup> deal with formation of a model to optimize a certain class of problems. Although these methods are more computationally efficient, obtaining an optimal solution is not guaranteed.

Deep learning (DL)-based design approaches, combined with limited exhaustive searches, have proven to be a potent solver of multi-objective optimization problems by learning the input–output relation.<sup>[21–36]</sup> DL-based approaches combined with dimensionality reduction (DR) algorithms have been recently developed for design and optimization of EM nanostructures.<sup>[20,37,38]</sup> More importantly, such novel techniques can provide considerable valuable insight about the dynamics of light–matter interaction in nanostructures with the hope of uncovering new physical phenomena that can be used to form

Y. Kiarashinejad, M. Zandehshahvar, S. Abdollahramezani, O. Hemmatyar, Dr. R. Pourabolghasem, Prof. A. Adibi  
Georgia Institute of Technology  
778 Atlantic Drive NW, Atlanta, GA 30332, USA  
E-mail: ali.adibi@ece.gatech.edu

 The ORCID identification number(s) for the author(s) of this article can be found under <https://doi.org/10.1002/aisy.201900132>.

© 2019 The Authors. Published by WILEY-VCH Verlag GmbH & Co. KGaA, Weinheim. This is an open access article under the terms of the Creative Commons Attribution License, which permits use, distribution and reproduction in any medium, provided the original work is properly cited.

DOI: 10.1002/aisy.201900132

completely new types of devices. Despite initial proof of principle,<sup>[37]</sup> there has been little effort on rigorously and systematically using these techniques to obtain detailed knowledge about the physics of light–matter interaction in EM nanostructures (e.g., MSs). The change in focus of using DL techniques from “optimization” to “knowledge discovery” can open a new research area with potentially transformative results in the entire field of nanophotonics. Examples of these “knowledge discovery” paradigms include assessing the feasibility of a desired response using a given structure as well as the range of possible responses a given design can provide. As existing optimization and inverse design approaches provide a solution to any inverse design problem and, to the best of our knowledge, such approaches have not considered the important concept of design feasibility, we believe our proposed method can pave the way for more efficient and practical and fabricationally favorable design paradigms. Knowing the feasibility of a desired response offered by a photonic nanostructure is very helpful prior to any design or optimization effort in avoiding suboptimal designs or convergence issues. It also guides us to modify the initial structure to achieve the desired response. To the best of our knowledge, this important concept has not been considered in existing optimization and inverse design approaches, which provide a solution to any inverse design problem regardless of its feasibility.

In this article, we present a new geometric deep learning (GDL)-based technique by forming the smallest convex set (i.e., the convex-hull)<sup>[39]</sup> to discover hidden optical phenomena while analyzing the feasibility of having a desired optical response from a certain class of EM nanostructures. GDL is a term used for techniques that aim to generalize DL approaches by considering the non-Euclidean domain such as manifolds. These methods reduce the dimensionality of the discovered patterns in the design and response space (RS) while finding the governing geometry of such patterns in lower-dimensional space (reduced space) in which the Euclidean distance can be a good measure for similarity of different patterns.<sup>[40–45]</sup> The developed approach in this article is based on reducing the dimensionality of the RS of a given EM nanostructure and finding the convex-hull that contains achievable responses in the reduced RS (also known as the latent RS). The DR implementation is based on an autoencoder,<sup>[46]</sup> and the Quickhull<sup>[47]</sup> algorithm is used to form the convex-hull in the latent RS. Our technique uses the numerical simulation of the response of the system for a series of randomly selected design parameters (called training set) and another series of similar simulations for validation of the technique. After initial training and validation, the algorithm finds the optimal bounded subset, which contains all feasible responses.

The optimal region that contains the feasible responses might not be convex in many cases, and it is better to also find a tighter bound over feasible responses in the latent RS. For this purpose, we use the one-class support vector machine (SVM) algorithm<sup>[48]</sup> to find the nonconvex geometry. One-class SVM also provides information about the level of feasibility (or unfeasibility) of a response and the possibility of trading an acceptable error (or a small change in the desired response) to get the closest feasible response to a unfeasible one (desired). Despite being implemented for the EM nanostructures (especially dielectric and plasmonic MSs), our technique can be applied to a wide variety

of applications once the training data can be provided. Some example extensions include thermal structures, fluidic systems, mechanical platforms, and acoustic metamaterials.

The rest of the article is organized as follows. Section 2 describes the details of the GDL-based approach. Section 3 demonstrates the application of the approach to two classes of important MSs. Section 4 is devoted to the comparison of the findings of our technique with experimental data. It is followed by the further discussions in Section 5 and conclusion in Section 6.

## 2. Theoretical Framework

### 2.1. Convex-Hull of a Set of Data Points

The convex-hull of a set of points is defined as the smallest convex set that contains all those points.<sup>[39]</sup> A  $d$ -dimensional convex-hull can be represented using its vertices and  $(d - 1)$ -dimensional facets. The ridges of the convex-hull are  $(d - 2)$ -faces, which are the intersections of the vertices in two neighboring facets. There are different algorithms presented in geometrical computation to form the convex-hull of a given set of points. One of the most effective and well-known algorithms is Quickhull, which forms the convex-hull using an incremental method based on Grunbaum's Beneath-Beyond theorem (see the Section 1, Supporting Information).<sup>[47]</sup> For a typical problem, the Quickhull algorithm starts with a set of given (or training) points and forms the initial convex-hull. The points that lie outside the initial convex-hull are considered as the outside set. The farthest point from the initial convex-hull (i.e., the point with the maximum Euclidean distance from its nearest facet) is found at each iteration, and the facets, ridges, and vertices are updated based on Grunbaum's Beneath-Beyond theorem.<sup>[47]</sup> These steps are repeated until the algorithm converges.

Although the convex-hull algorithm is capable of finding a convex geometry for feasible responses, it has some limitations. If the optimum feasible region is not convex, inevitably some unfeasible regions in the latent RS will be included in the convex-hull to reach a convex region. This limits the efficiency of the algorithm for such structures due to the false-positive errors. Moreover, the algorithm acts as a binary classifier and classifies responses into two classes: feasible (achievable) and unfeasible (unachievable). In most practical cases, it is desirable to know how far an unfeasible response is from feasible responses. It is also helpful to know whether it is possible to push an unfeasible response toward the feasible region by accepting some error. Unfortunately, the Euclidean distance of a given point in the latent RS from the boundaries of the convex-hull is not a good measure for feasibility of the corresponding response. To address this limitation, we use one-class SVM in the latent RS as the alternative algorithm.

### 2.2. One-Class SVM for a Set of Data Points

One-class SVM is an algorithm that separates the patterns into two regions (e.g., feasible and unfeasible in our case). In addition, the Euclidean distance between any point in the space and the boundaries of the one-class SVM is a good measure of this separation (e.g., a good measure of the feasibility of a

response in our case). Mathematically, a one-class SVM forms a nonlinear geometry by projecting patterns  $x_i$  through a nonlinear function  $\phi$  to a higher-dimensional space  $F$ . This mapping helps to separate linearly nonseparable patterns in the low-dimensional input space  $I$  in high-dimensional space by a hyperplane (represented with  $w^T + b = 0$ ,  $w \in F$ , and  $b \in \mathbb{R}$ ). By projecting this hyperplane from the high-dimensional space back to the original space, the algorithm finds the equivalent nonconvex decision geometry. In this projection, the resulting region for the desired (or feasible) class of data may not only have a nonconvex geometry but it may also exclude smaller closed regions within the geometry. The implementation of the one-class SVM has considerable flexibility through two parameters  $\nu$  and  $\gamma$  which control the tightness of the geometry of the decision region and the maximum ratio of the given training patterns that fall outside the geometry (and thus contribute to the classification error). Using different values of  $\gamma$ , one can find a series of boundaries with different levels of classification errors for the ground-truth data. Although one-class SVM is capable of finding the nonconvex geometry of latent patterns, computation complexity of validating  $\nu$  and  $\gamma$  in each iteration prevents using it as a preliminary approach of forming the geometry in many cases. Using the convex-hull forming algorithm to get the initial information for implementing the one-class SVM algorithm is a very effective solution to this challenge. Further details about the one-class SVM are provided in the Section S2, Supporting Information.

### 2.3. Investigation of the Feasibility of a Desired Response from a Given Structure

Figure 1a shows the schematic of our technique for forming the convex-hull for the feasible responses of a given nanostructure. In the first step, a full-wave EM simulation software (or alternatively an EM wave solver using an analytic or a semi-analytic model) is used to provide an initial batch of randomly generated patterns (we refer to them as the input dataset). Each pattern is calculated using a given set of randomly selected design parameters (i.e., a point in the design space [DS]), and thus it relates the DS to the RS. Then, we reduce the dimensionality (see Section S3, Supporting Information) of the RS by training an autoencoder using a subset of the available training data and a desired autoencoder reconstruction error. Next, we use the Quickhull<sup>[47]</sup> algorithm to form a convex-hull to bound the patterns in the latent RS. Then, we validate the convex-hull using a batch of validation data. As all of the validation responses originate from a feasible structure, the optimum convex-hull should bound all the validation data. We put a threshold for the validation success rate. If the convex-hull does not pass the validation step, the validation batch will be added to the initial training batch to expand the training dataset for retraining the algorithm. This process is repeated until the resulting convex geometry reaches the desired validation success rate. After convergence, the convex geometry is tested using an unseen test dataset (that includes both feasible and unfeasible responses) to find its performance defined by the error rate. A similar process is used for training the one-class SVM as shown in Figure 1b to find the nonconvex geometry of feasible response patterns in the latent RS.

### 3. Response Feasibility Investigation

To demonstrate the potentials of our technique, we apply it to the investigation of possible optical reflection responses from plasmonic and dielectric MSs as two popular classes of photonic nanostructures. Figure 2a,b shows two implementations of a digital plasmonic MS consisting a  $7 \times 7$  and a  $14 \times 14$  array of binary nanocubes of stacked aluminum/alumina (Al/Al<sub>2</sub>O<sub>3</sub>), respectively. The significant number of plasmonic inclusions or design parameters, especially that in Figure 2b, allows these structures to form sophisticated EM responses such as Fano and Lorentzian resonances.<sup>[49,50]</sup> As an alternative, we also consider a median-index dielectric MS formed by a square lattice array of hafnia (HfO<sub>2</sub>) nanoparticles on a transparent substrate as shown in Figure 2c. For both classes of MSs, we train a convex-hull and a one-class SVM to quantitatively evaluate the practical feasibility of any desired response based on a small set of simulation results found by calculating the reflection spectrum of the MS in the visible wavelength range using the FEM implemented in a commercial full-wave package COMSOL Multiphysics as explained in Section 7.

The design patterns in each case are achieved by random selection of the binary inclusions, and the calculated reflection spectra are sampled uniformly in the 400–800 nm wavelength range with 2 nm resolution to form a vector with dimensionality of 200 as the response pattern. Due to the iterative nature of the algorithm in Figure 1a, the minimum number of training data depends on the number of iterations for convergence. In addition, we use 500 simulated response patterns for testing the algorithms after convergence. Based on several simulations to understand the requirement of the selected structure, we chose 8000 as the size of the training/validation dataset. Knowing that achieving an ideal Fano lineshape is not possible with these structures (due to remarkable Ohmic loss of metals in the visible range), we also formed 80 ideal Fano lineshapes over the 400–800 nm spectral using the Equation S(8) (see Section 5, Supporting Information) as unfeasible responses to test the algorithms.

After obtaining the training dataset, the first step of implementation is the DR of the RS by training an autoencoder. To find the optimum dimensionality of the latent RS and the number of layers of the autoencoder, we use an ad hoc approach using different autoencoder structures and dimensionalities and calculating the mean squared error (MSE) for each case. The details of this approach are explained in the study by Kiarashinejad et al.<sup>[37]</sup> and not repeated here. Figure 3a shows the variation of the MSE of the autoencoder trained for the  $14 \times 14$  array in Figure 2b with the dimensionality of the latent RS. The autoencoder in each case is compared to seven layers with 200, 100, 50, X, 50, 100, and 200 neurons, with X being the dimensionality of the latent RS. Training and testing the autoencoder are performed with 8000 and 2000 random response patterns, respectively. Figure 3a shows that using 6 as the dimensionality of the latent RS results in MSE of 0.001, which can be translated to less than 5% point-to-point error (see Section S3, Supporting Information).

It is important to note that the goal of this initial training step is to find the optimum dimensionality of the autoencoder in Figure 1. For optimal training of either algorithms in Figure 1a,b, we use an untrained autoencoder with the optimum

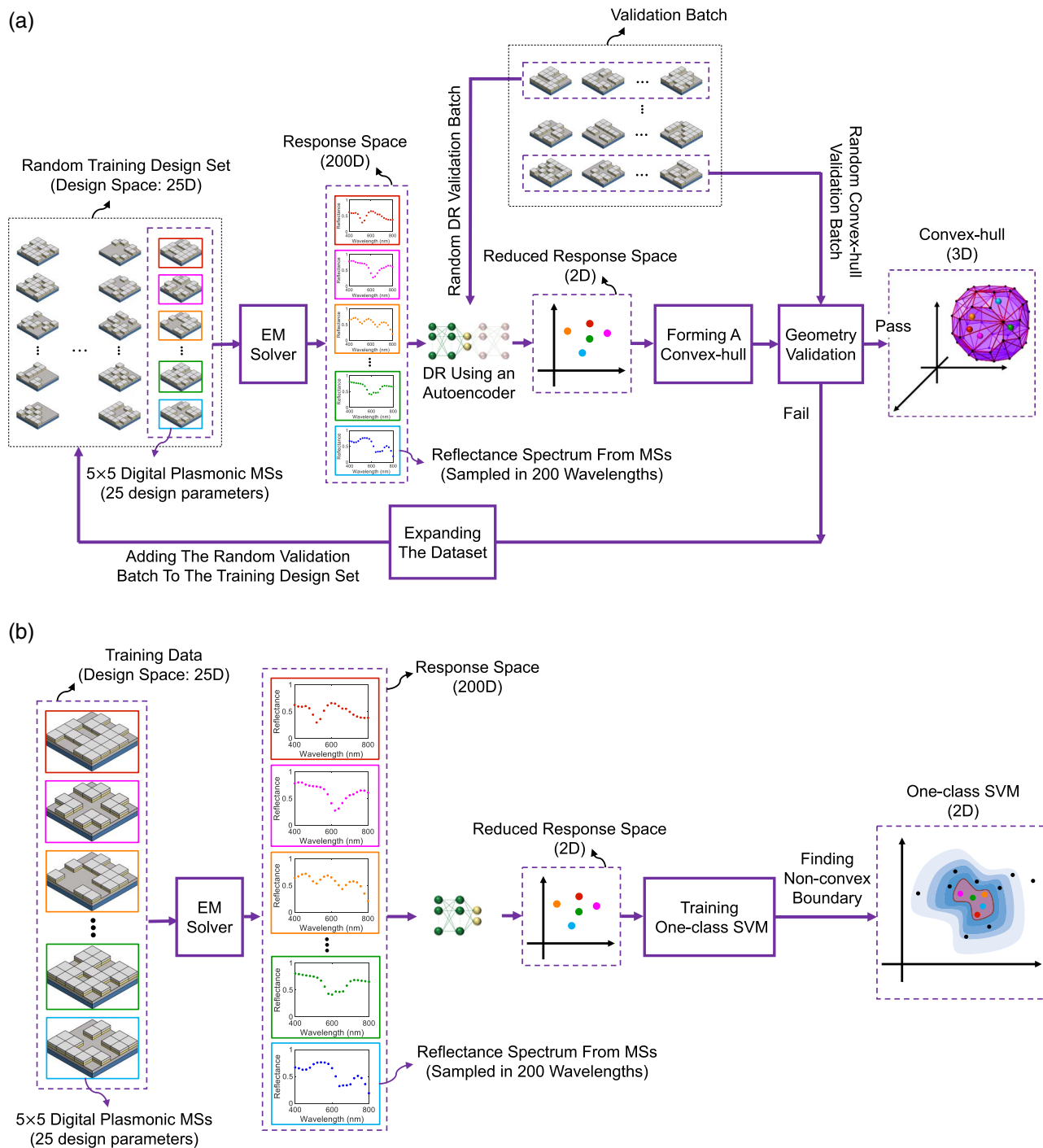


**Figure 1.** a) Training algorithm for finding the convex-hull of the patterns in the latent RS. b) Using one-class SVM over patterns in the latent RS to investigate the level of feasibility of a desired response. The dimensionality of the latent RS is found by training the autoencoder. The 2D and 3D representations are just examples for facilitating graphical understanding.

dimensionality and train the entire algorithm (composed of the autoencoder followed by the Quickhull to form the convex geometry). To find the optimum convex-hull in the resulting latent RS, we start with an initial batch of data with 5000 ground-truth patterns in the algorithm in Figure 1a (with dimensionality of RS being 6) to train the cascaded autoencoder and forming the

convex-hull in the 6D latent RS space. At each iteration, we use 200 validation data (without replacement) for autoencoder and 200 for convex-hull. We select 0.001 (5% point-to-point error) for the autoencoder validation threshold and 95% for in-point percentage (i.e., percentage of the ground-truth patterns lies inside the boundary), respectively. The algorithm converged after

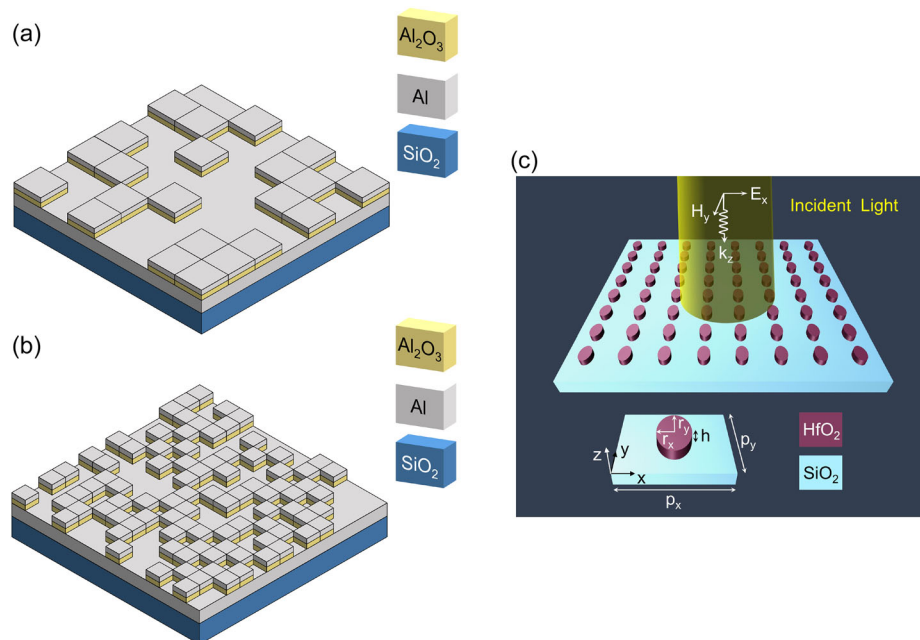


**Figure 2.** a,b) The schematic of a unit cell of a digital plasmonic MS composed of a square lattice of (a)  $7 \times 7$ , and (b)  $14 \times 14$  binary inclusions. The substrate consists of an Al layer as the back reflector covered by an array of Al/ $\text{Al}_2\text{O}_3$  binary inclusions. The thickness of the deposited Al back-reflector, Al, and  $\text{Al}_2\text{O}_3$  layers in both cases are 100, 35, and 35 nm, respectively. c) The unit cell of a median-index dielectric MS consisting of  $\text{HfO}_2$  nanopillars, deposited using ALD with the optical properties reported in the study by Devlin et al.<sup>[51]</sup> The structure is normally illuminated by a TM-polarized EM wave (TM, i.e., magnetic field in the plane of the inclusions), as shown in (c), and the reflection response is calculated and sampled over the bandwidth of 400–800 nm to be introduced to the algorithms in Figure 1.

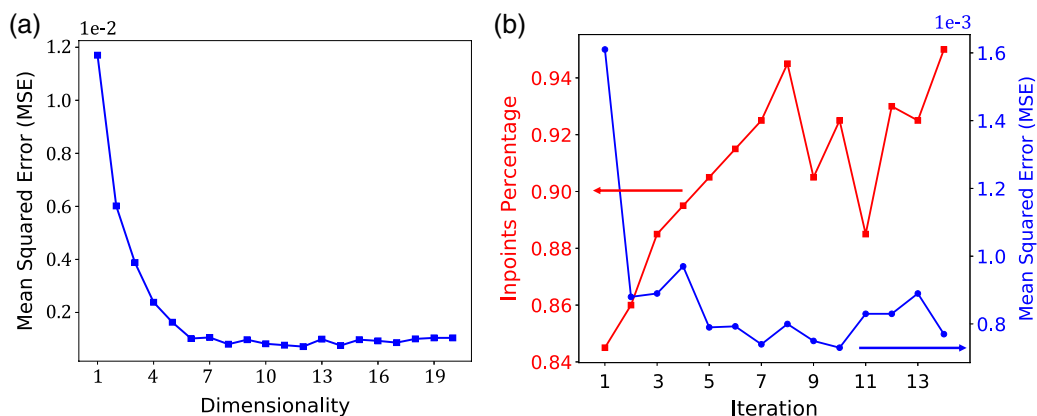


**Figure 3.** a) Reconstruction MSE for autoencoder trained on the responses of the  $14 \times 14$  binary structure in Figure 2a for different dimensionalities of the latent RS. Using the results, we select 6 as the desired dimensionality of the latent RS. Responses can be reconstructed after reducing dimensionality from 200 to 6 by accepting less than 5% error. Examples of reconstructed responses and the ground truth responses are presented in the Section 4, Supporting Information. b) Auto-encoder training error and in-points percentage for the algorithm in Figure 1a for  $14 \times 14$  binary structure in Figure 2a after different iterations of the algorithm. The algorithm converged after 14 iterations.

14 iterations. As a result, we used 11 000 data to reach convergence.

Figure 3b shows the MSE of the autoencoder and percentage of ground-truth test data that lie in the convex-hull after each iteration. After validating the convex-hull and its corresponding autoencoder, we feed our test data consisting of feasible responses for the  $14 \times 14$  and  $7 \times 7$  binary nanostructures as well as unfeasible ideal Fano resonances to the algorithm.

The results (see **Table 1**) show that about 91.8% of the feasible responses of the  $14 \times 14$  structures, 96% of those of the  $7 \times 7$  structures, and none of the unfeasible Fano resonances are enclosed by the convex-hull. To provide a visual perspective of the convex-hull, we repeat the algorithm in Figure 1a in 2D and 3D latent RS (dimensionality of the response RS being 2 and 3, respectively). We set 0.005 and 0.0035 as the autoencoder validation error (10% and 7% point-to-point error) for 2D and

**Table 1.** In-points percentage of each class of test patterns ( $14 \times 14$  and  $7 \times 7$  responses as well as Fano line-shape resonances) lies in the 2-D, 3-D, and 6-D convex-hull as well as one-class SVM highest confidence region.

Algorithm class	Binary $14 \times 14$ [%]	Binary $7 \times 7$ [%]	Fano lineshapes [%]
Convex 2-D	99.2	100	35
Convex 3-D	98.6	99.8	10
Convex 6-D	91.8	96	0
One-class SVM 2-D	90.2	90.6	0
One-class SVM 3-D	91.4	89.4	0
One-class SVM 6-D	88.2	84.8	0

3D spaces, respectively, while using 95% as the in-point percentage threshold for both spaces. **Figure 4a,b** shows the converged convex-hulls in 2D and 3D latent RSs; the calculated errors in testing the resulting convex-hulls are shown in Table 1.

It is clear from Table 1 that both 2D and 3D algorithms are capable of identifying the feasible responses with better than 99% accuracy, but their ability in identifying the unfeasible responses are reduced (from 0% to 10% and 35%, respectively). In other words, by reducing the dimensions, it seems that the convex-hull covers a larger percentage of the overall area of the latent RS resulting in a larger error in identifying the unfeasible responses.

It is important to note that despite training with a nonaggressive success rate of 95%, the convex-hull algorithm is capable of identifying all unfeasible responses as well as a large portion of the feasible responses. Nevertheless, the convex-hulls in Figure 4 do not provide the level of feasibility or unfeasibility of a response. For example, it is not trivial to compare the robustness of the resulting designs for achieving two responses as there is not a simple one-to-one relation between the Euclidean distance to the convex-hull boundary and the feasibility of a response. To add this feature, we use the same training/validation data to train a one-class SVM to find the nonconvex geometry of

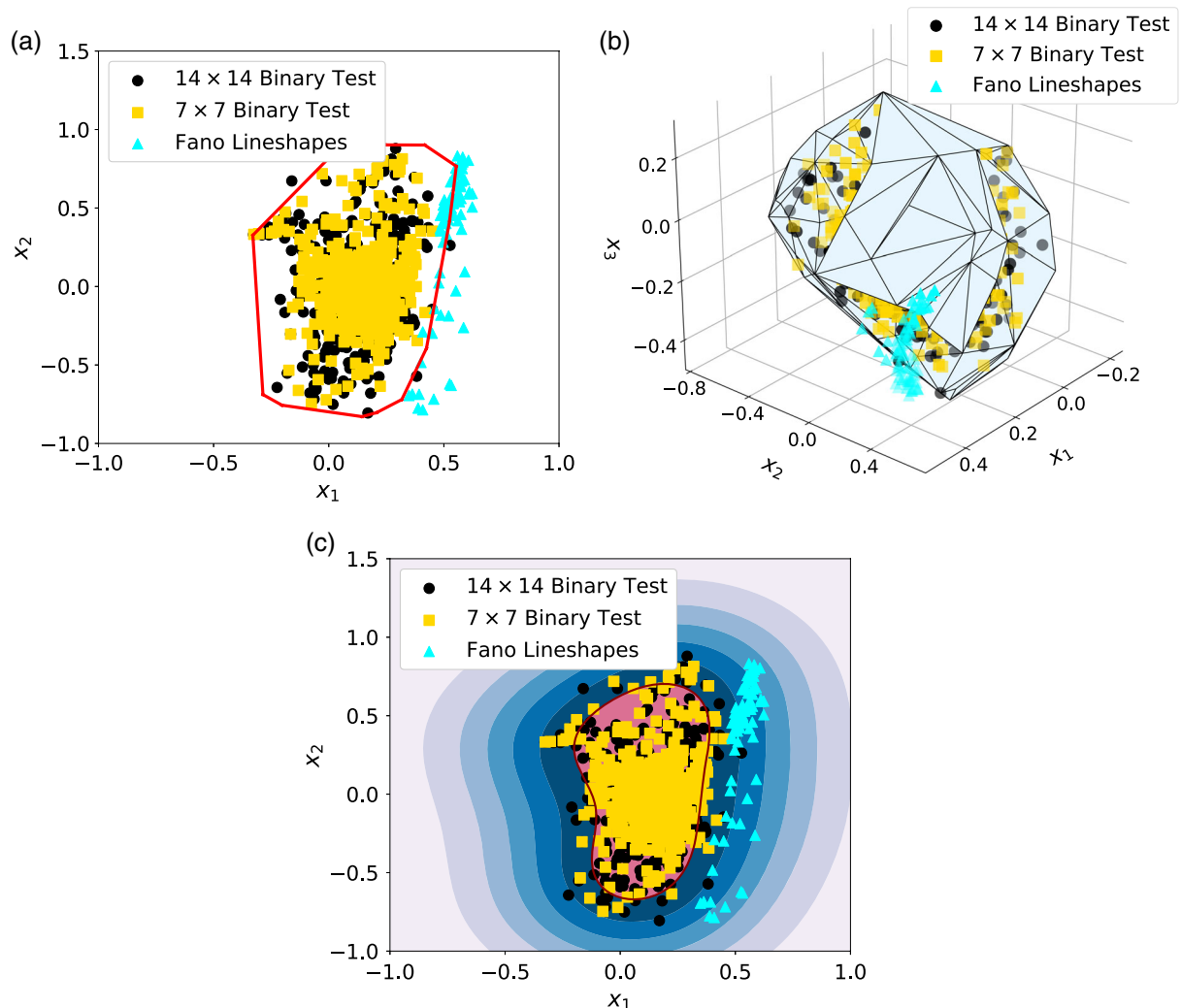


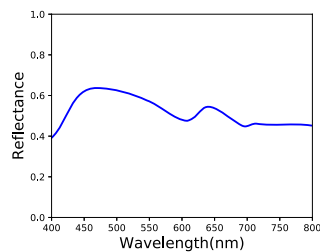
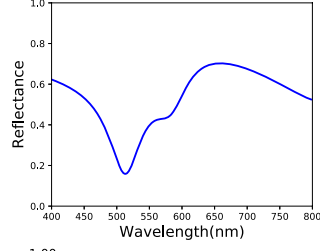
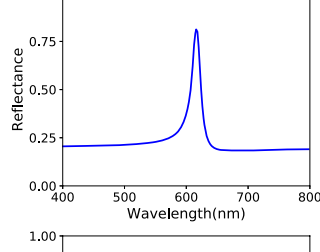
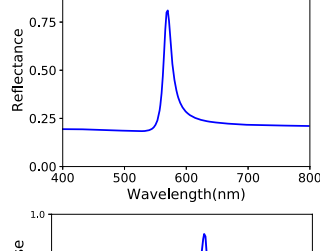
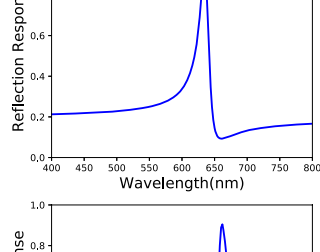
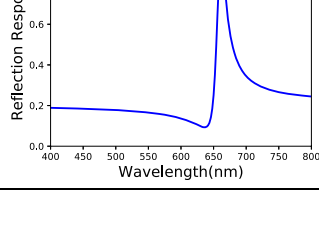
**Figure 4.** Representation of the convex-hulls in a) 2D and b) 3D RS space of the  $14 \times 14$  binary structure in Figure 2b. The feasible responses for the  $14 \times 14$  and  $7 \times 7$  binary structures and the unfeasible ideal Fano lineshapes are shown. c) Nonconvex geometry for the feasible responses found by one-class SVM algorithm along with feasible and unfeasible responses in the 2D latent RS for the  $14 \times 14$  binary structure in Figure 2b.

the feasible responses for the structure in Figure 2a using 6D, 3D, and 2D latent RSs. Although one-class SVM provides valuable information about the relative feasibility of each desired response, finding the optimum hyperparameters (i.e.,  $\nu$  and  $\gamma$ ) for one-class SVM is challenging. Here we use 500 validation patterns to cross validate the hyperparameters and find  $\nu = 0.4$  and  $\gamma = 4$  as the optimum parameters. Table 1 shows the results of testing the 6D, 3D, and 2D one-class SVM algorithms with the same data used for testing the convex-hull algorithm. Smaller success rates in identifying the feasible responses while perfect performance in identifying unfeasible responses are attributed to the tighter (nonconvex) geometry of the one-class SVM. This is also seen from the graphical representation of the one-class SVM in the 2D latent RS in Figure 4c. Note also that the absolute values of the success rates in Table 1 for one-class SVM depend on the definition of the highest confidence region. Reducing the level of confidence results in extension of its corresponding geometry and thus a smaller error. In addition to the innermost geometry (also known as the highest confidence geometry) shown by the red curve in Figure 4c, several boundaries are identified with different colors. Each added region corresponds to a different level of unfeasibility of a response that lies outside the highest confidence region. A quantitative measure for the level of feasibility of a response in this one-class SVM is the minimum Euclidean distance of that response from the boundaries of the highest confidence region. The calculated distance in the 6D one-class SVM for a series of responses of the structure in Figure 2a is shown in Table 2. The average distance for each class of responses in Table 2 is calculated over the entire set of those responses in the test dataset. In addition, for each class, a representative sample response and its actual distance from the geometry are shown. A negative (positive) distance shows that the point lies outside (inside) the highest confidence region; the absolute value of the distance shows the relative unfeasibility (feasibility) of a response. Table 2 clearly shows that a smoother response (e.g., the first row of Table 2) has a better feasibility than a sharper one (second row of Table 2). It also confirms the unfeasibility of the ideal Fano and Lorentzian responses with Fano responses being farther from the feasibility region.

## 4. Experimental Results

To show the applicability of our technique in practical problems, without loss of generality, we choose a reflective structure formed by a low-loss dielectric ( $\text{HfO}_2$ ) MS (2(c)), which can be experimentally fabricated and characterized. The training data for this structure are found by simulating the constituent unit cell with different geometrical parameters using FEM implemented in the COMSOL Multiphysics (see Section 7). The dimensions of the unit cell ( $p_x$  and  $p_y$  in Figure 2c) can be changed between 250 and 450 nm, whereas the radii of the nanopillars are proportionally modified ( $r_x$  and  $r_y$  in Figure 2c) from  $r_{x,y} = 0.6p_{x,y}$  to  $r_{x,y} = 0.75p_{x,y}$ . The structure is illuminated by a transverse magnetic (TM)-polarized plane wave of light at normal incidence, and the reflection coefficients at the far-field are calculated over the range of 400–800 nm wavelength range for 2400 patterns. The reflection spectra are uniformly sampled at 200 wavelengths to form a 200-dimensional RS. The resulting data are used to

**Table 2.** Average distance of different classes of test data ( $14 \times 14$  and  $7 \times 7$  responses as well as Fano and Lorentzian lineshape resonances) from the highest confident region border for one-class SVM. Distances for random samples represented in the most right column are also represented. The distances are calculated using Equation S(8), Supporting Information.

	Average distance	Sample distance	Sample plot
Binary $14 \times 14$	60.89	128.44	
Binary $7 \times 7$	56.08	15.36	
Lorentz shape 1	−74.57	−62.53	
Lorentz shape 2	−72.70	−46.75	
Fano shape 1	−85.02	−60.71	
Fano shape 2	−80.39	−117.51	



form the convex-hull and one-class SVM of the MS using the algorithms in Figure 1. The convex-hull-forming algorithm starts with an initial batch of data of 1000 patterns to train the autoencoder and form the 2D and 3D convex-hulls. In each iteration, we use 200 validation data for the autoencoder and 200 for the convex-hull. We select 5% and 95% as the validation thresholds for the autoencoder MSE and in-point percentages for the convex-hull, respectively. The algorithm converges after 5 (7) iterations for 2D (3D) RS space. After convergence, we test the algorithm using 200 ground-truth patterns whose results are shown in Figure 5a,b. We also train a one-class SVM with  $\nu = 0.4$  and  $\gamma = 0.1$ , and the results are shown in Figure 5c. Our calculated in-points rate for the 2D (3D) convex-hull and the one-all SVM over the entire test data are 100% (98.5%) and 93.5% (93%), respectively. Table 3 compares the average distance of test response patterns from the boundary formed using one-class SVM for simulation and experiment. The results show that the algorithm is capable of providing a feasible geometry for experiment while it is trained on simulation data.

**Table 3.** Average distance of test patterns for the responses achieved from nanopillars to the formed geometry of one-class SVM (using the training data achieved from the simulation patterns).

Algorithm type	Simulation	Experiment
One-class SVM 2-D	3.655	3.657
One-class SVM 3-D	2.343	2.560

To evaluate the convex-hull experimentally, we fabricated several dielectric MSs with symmetric unit cells (i.e.,  $p_x = p_y = p$ ) with  $250 \text{ nm} < p < 450 \text{ nm}$  consisting of symmetric nanopillars (i.e.,  $r_x = r_y = r$ ) with  $0.65p < r < 0.75p$  (see Experimental Section for the fabrication details). The scanning electron microscopy (SEM) image for a fabricated MS with  $p = 450 \text{ nm}$  and  $r = 0.75p$  is shown in Figure 6a,b shows a good agreement between the simulated and measured reflectance. Figure 7 shows the placement of the experimentally measured responses in the RS

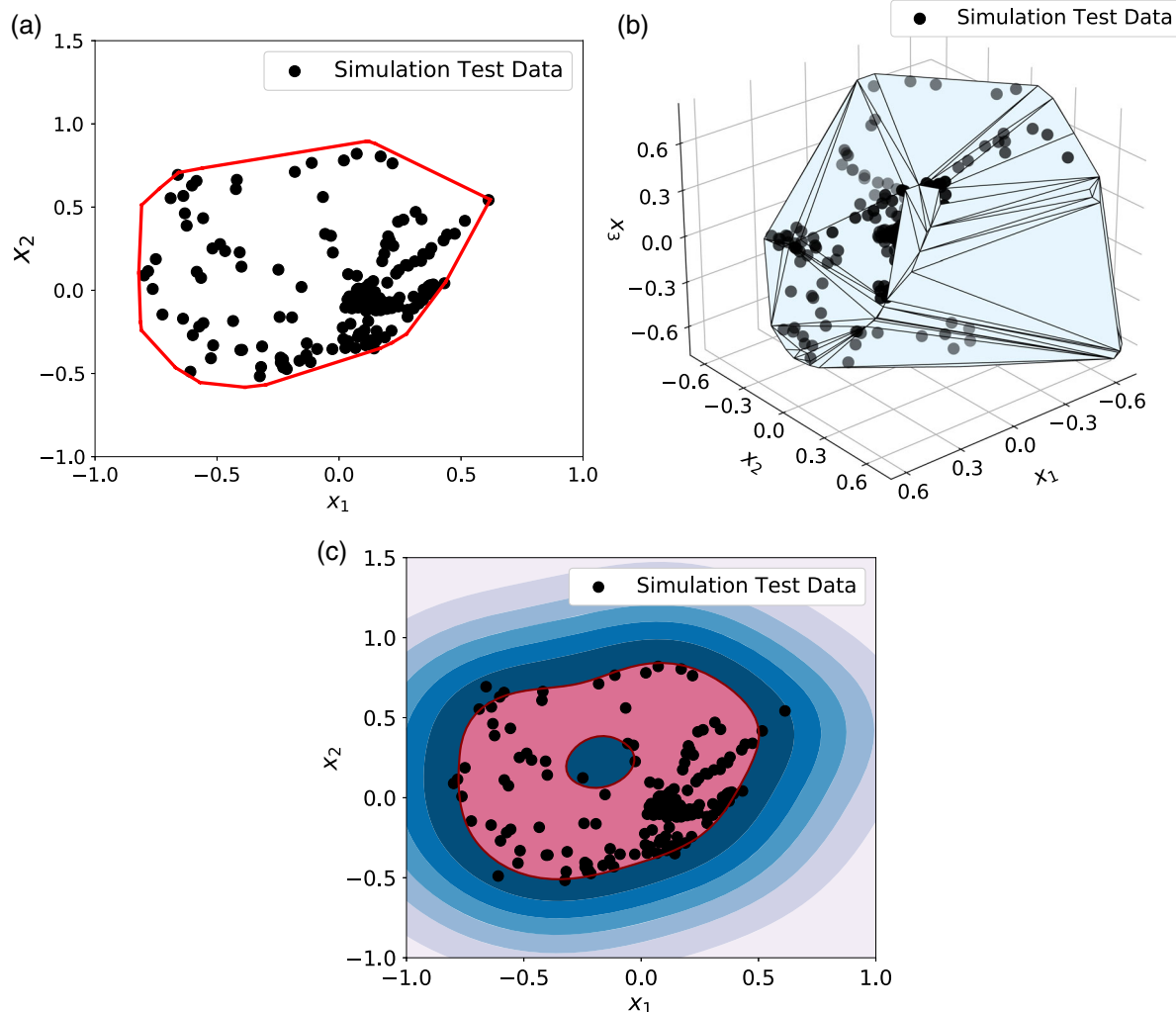


**Figure 5.** Representation of the a) 2D convex-hull, b) 3D convex-hull, and c) one-class SVM for the  $\text{HfO}_2$ -based MS in Figure 2c. The simulated structure consists of a square lattice of  $\text{HfO}_2$  nanopillars with  $p_x = p_y = p$  (ranging from 250 nm to 450 nm) and radii  $r_x = r_y = r$  ( $0.6p < r < 0.75p$ ). The feasible test patterns are also shown in each case demonstrating the capability of these algorithm in encompassing the feasible responses.



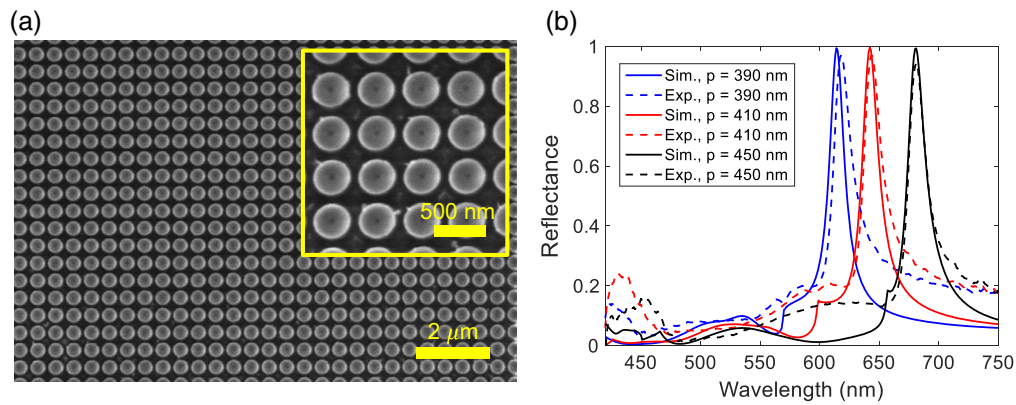


**Figure 6.** a) SEM images of a fabricated MS consisting of a rectangular lattice of cylindrical  $\text{HfO}_2$  nanopillars with periodicity  $p_x = p_y = p = 450$  and radii  $r_x = r_y = r = 0.75p$  ( $p_x, p_y, r_x, r_y$  are defined in Figure 2(c)). b) The simulated and experimentally measured (Exp) reflectance spectra from MS (similar to the one in (a)) with periodicities  $p = 390, 410$  and  $450$  nm and nanopillars with radii  $r = 0.75p$ .

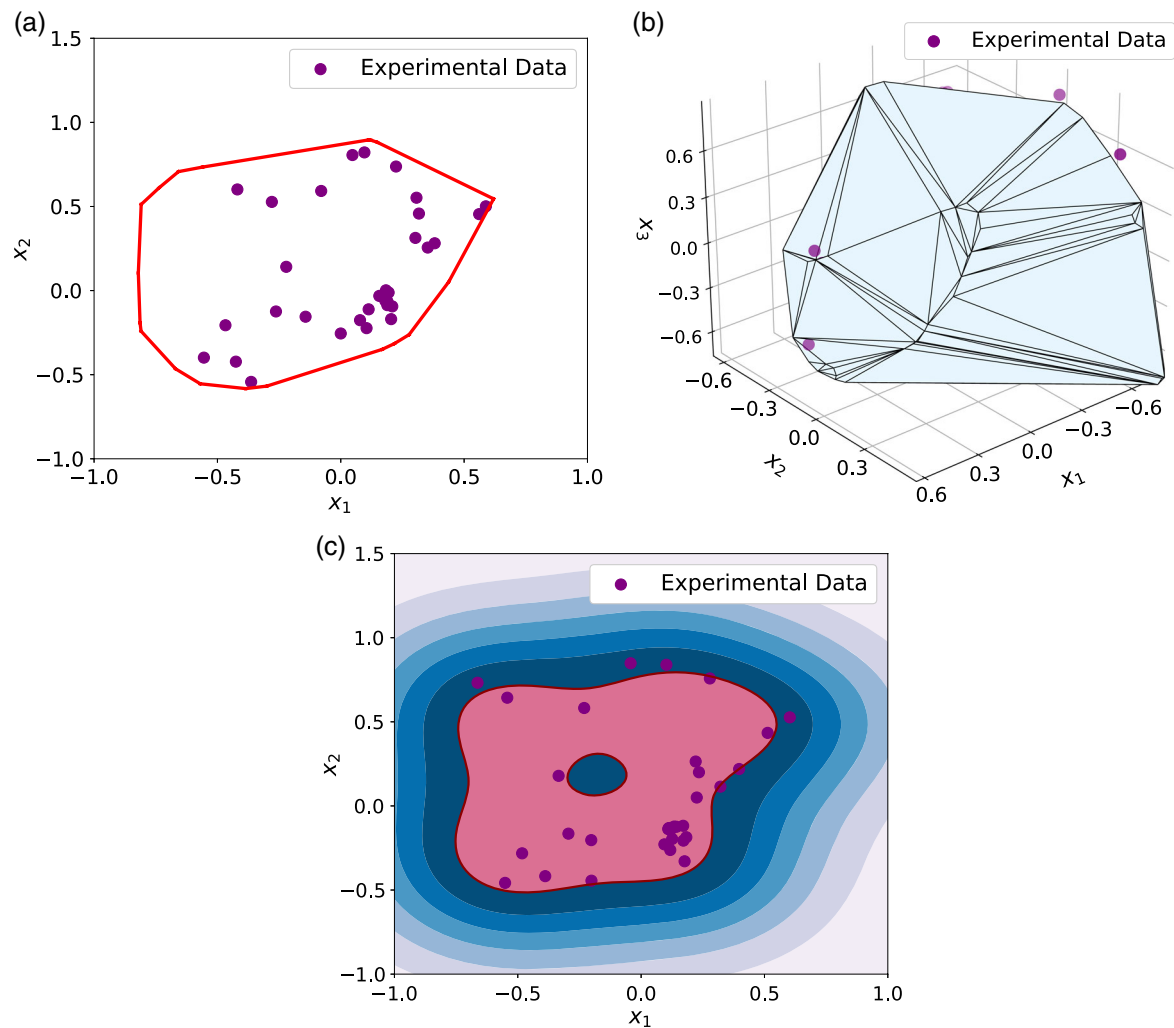


**Figure 7.** a) 2D convex-hull, b) 3D convex-hull, and c) 2D one-class SVM for the dielectric MSs shown in Figure 2 with properties described in the caption of Figure 6. The experimentally measured data also shown. It is clear that almost all experimental results fall within the convex-hull or one-class SVM boundaries.

space of the structure. It is clear that a large portion of the feasible responses fall within the convex-hull and the one-class SVM. In addition, the responses that fall outside the one-class SVM are close to the geometry of the highest confidence geometry with small distances. The calculated success rates of the 2D (3D) convex-hull and the one-class SVM in Figure 7 for the experimental results are 100% (87.8%) and (87.87%) (81.81%), respectively, which is in good agreement with the theoretical results. Note that the despite using low dimensions for the latent RS, our techniques provide good success rates in identifying the feasible responses.

## 5. Discussion

The results in Figure 4, 5, and 7 and Table 1–3 clearly show the power of GDL algorithms in assessing the feasibility of a desired response given a specific nanostructure design. They also show the advantage of one-class SVMs in providing a more quantitative measure for the level of feasibility of the desired response. This advantage comes from the fact that in one-class SVM, the geometric distance of a point in the latent RS from the boundaries of the one-class SVM is a good measure for the feasibility of the response, whereas in convex-hulls, this relation does not hold necessarily. This advantage comes at the expense of more sophisticated training as the optimum hyperparameters  $\nu$  and  $\gamma$  in SVM are not usually trivial to find. In practice, we first find the convex-hull of the feasible responses and use it to find proper values of  $\nu$  and  $\gamma$  as explained in Section S2, Supporting Information. Nevertheless, convex-hulls are helpful in providing the quick evaluation of the feasible response feasibility. The training process can also be simplified if more error is accepted. Note also that finding the exact geometry of the convex-hull and one-class SVM may not be important in design and optimization problems as the points on the boundaries correspond to less reliable responses that are prone to environmental changes or fabrication errors. We prefer the desired response to be in the middle of the one-class SVM.

In addition to the boundaries of convex-hull and one-class SVM in the latent RS, the area that is covered in that space

by these shapes has important practical implications. The larger the area, the more capable the structure is in forming varieties of output responses. Figure 8a and b shows convex-hull and one-class SVM, respectively, in the 2D latent RS of the binary MS structure in Figure 2a formed by  $7 \times 7$  array of nanostructures. For comparison, the responses used for the testing of the  $14 \times 14$  structure in Figure 2b are also provided. For comparison, Figure 4a,c shows the 2D convex-hull and one-class SVM, respectively, for the  $14 \times 14$  structure while the testing data for the  $7 \times 7$  structure also presented. It is clear from Figure 4 and 8 that the convex-hull and one-class SVM of the  $7 \times 7$  structure cover a smaller percentage of the 2D latent RS than those of the  $14 \times 14$  structure. This conclusion must be taken with the caveat that the latent RSs for the two structures are not necessarily the same. Note that a wider range of responses may or may not be desirable for a design. For reconfigurable structures, a wider response range is an advantage, whereas for devices with a specific functionality, wider response range usually is considered as unnecessary complexity of the selected structure. Figure 4 clearly shows that while technically none of the responses of the  $7 \times 7$  structure was used in training the convex-hull and one-class SVM of the  $14 \times 14$  structure, all these responses fall inside the convex-hull and one-class SVM as any  $7 \times 7$  structure can be formed using the  $14 \times 14$  structure. Figure 8a,b also shows that some of the responses achieved by the  $14 \times 14$  structure cannot be achieved using the  $7 \times 7$  structure, whereas some of them can. This is an important observation as it confirms that using the  $14 \times 14$  structure for some responses might be unnecessary; the same response can be achieved by a much simpler structure (e.g.,  $7 \times 7$  structure in this case) with less fabrication challenges and more robustness against fabrication imperfection. We believe this observation is an important potential application of convex-hull and one-class SVM in finding the most robust and least complex structures when starting from a nonoptimal design. In addition, selecting a structure for which the desired response falls in the middle of the one-class SVM (i.e., has maximum distance from the boundaries) results in more tolerance against environmental changes and fabrication imperfections.

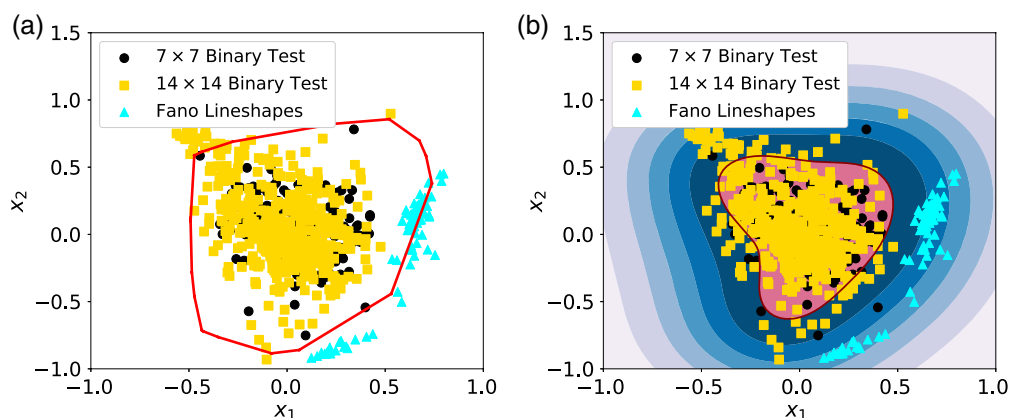


**Figure 8.** Representation of the convex-hulls in a) 2D RS space of the  $7 \times 7$  binary structure in Figure 2b. The feasible responses for the  $7 \times 7$  and  $14 \times 14$  binary structures and the unfeasible idea Fano lineshapes are shown. b) Nonconvex geometry for the feasible responses found by one-class SVM algorithm along with feasible and unfeasible responses in the 2D latent RS for the  $7 \times 7$  binary structure in Figure 2b.

The DR algorithm implemented by the autoencoder is an important step in reducing the required computational resources for the convex-hull and one-class SVM. For any particular problem, the optimum dimension of the latent RS depends on the selection of the design and the redundancy of the response (i.e., the level of nonuniqueness). Thus, finding the optimum size of the latent RS is the initial step in implementing the algorithms of this article. Once the size of the latent RS is selected, the required computation for the calculation of the convex-hull and one-class SVM is primarily for the training algorithm. In this article, we mainly used the brute-force approach in starting with a training dataset and expanding it until the convex-hull (and subsequently the one-class SVM) pass the validation test. Further rigorous approaches must be developed to minimize the computation required for training. One can also take advantage of the trade-off between the accuracy (or the error) and the computation requirement to optimize the training approach as explained earlier.

Although the focus of this article was the first demonstration of a GDL-based technique for studying the feasibility of a given response, this technique can be adopted for obtaining far more detailed information about the physics of nanostructures. As an example, Figure 4 clearly shows that the Fano-type resonances are clustered separately from the non-Fano resonances. Further extension of this technique to separate more classes of responses (known as clustered homotops) is currently under investigation.

Our approach can also facilitate the design of nanostructures using conventional inverse problem-solving approaches such as genetic algorithms that focus on finding the design parameters of a selected structure without carefully studying the feasibility of achieving the desired response using the selected design. These techniques can use our approach as an initial feasibility study step to ensure the selected structure for the optimization process is indeed a proper choice. More importantly, our approach can help reducing the complexity of the initial selection (as explained earlier) before running the optimization procedure to avoid unnecessarily complex designs and reduce the fabrication challenges. We believe our approach can be optimally combined with our newly demonstrated DL-based design algorithm,<sup>[20]</sup> which can provide global optimum while addressing the nonuniqueness issue in typical EM design problems.

## 6. Conclusions

In summary, we presented here a new approach to utilize artificial intelligence (AI) for knowledge discovery in nanophotonics through training two well-known algorithms (convex-hull and one-class SVM). We showed that by combining the convex-hull (or one-class SVM) with DR by an autoencoder, we can find the range of feasible responses as well as the degree of feasibility of a desired response from any given class of EM nanostructure in its latent RS. By applying these techniques to a series of MSs, we showed the unique capabilities of one-class SVM and convex-hull in providing valuable insight about the capabilities of any EM nanostructure in providing different types of responses. Although this is the first demonstration of an AI-based approach for such knowledge discovery, the presented

techniques show great potentials in facilitating the understanding of the underlying physics of EM nanostructures as well as forming a more systematic approach in designing such nanostructures.

## 7. Experimental Section

**Numerical Simulations:** All the simulations of the presented GDL method (including Quickhull, autoencoder, and one-class SVM) were implemented in Python using a simple personal computer with a 3.4 GHz core i7-6700 CPU and 16 GB of random access memory (RAM). The numerical simulations throughout the article were conducted using the FEM implementation in COMSOL Multiphysics environment and interfaced to MATLAB to facilitate the process. For the design of single unit cells of any structure, periodic boundary conditions and perfectly match layers were considered in the lateral and vertical directions, respectively. A TM-polarized light in the range of 400–800 nm was launched into the simulation domain, and the copolarized reflection coefficient was calculated at the location of the input port over the input bandwidth. The optical constants of Al, Al<sub>2</sub>O<sub>3</sub> in Figure 2a,b were obtained from the previous study by Palik<sup>[52]</sup> using tabulated dielectric functions. The measured ellipsometry data for HfO<sub>3</sub> and quartz were used to simulate the structure in Figure 2c.

**Fabrication Process:** The dielectric MS shown in Figure 6a was fabricated on top of a quartz substrate. First, the substrate was cleaned and exposed to an oxygen plasma, followed by spin coating of a positive-tone electron-beam (e-beam) resist (ZEP-520A). The substrate was then soft baked and coated with a conductive layer of Espacer to prevent charging effects during the e-beam writing process. Then, the sample was exposed to the e-beam (ELS-G100) to write the patterns, followed by development in the diluted amyl acetate liquid. Atomic layer deposition (ALD) of HfO<sub>2</sub> was performed using a standard two-pulse system of water and TEMA<sub>4</sub> at 90° under continuous flow of nitrogen carrier gas (Cambridge Nanotechnology). In the next step, the deposited top HfO<sub>3</sub> layer was etched using the inductively coupled plasma-reactive ion-etching process to reach the top surface of nanostructures. Finally, the sample was exposed to the ultraviolet light and oxygen plasma and soaked in the 1165 remover to remove the residue of the e-beam resist.

## Supporting Information

Supporting Information is available from the Wiley Online Library or from the author.

## Acknowledgements

The work was funded by Defense Advanced Research Projects Agency (DARPA) (D19AC00001, Dr. M. Fiddy), and was performed in part at the Georgia Tech Institute for Electronics and Nanotechnology, a member of the National Nanotechnology Coordinated Infrastructure (NNCI), which was supported by the National Science Foundation (ECCS-1542174).

## Conflict of Interest

The authors declare no conflict of interest.

## Keywords

artificial intelligence, deep learning, light–matter interactions, machine learning, nanophotonics

Received: October 30, 2019  
Revised: November 17, 2019  
Published online: December 19, 2019

- [1] F. Ding, A. Pors, S. I. Bozhevolnyi, *Rep. Progress Phys.* **2017**, *81*, 026401.
- [2] S. M. Kamali, E. Arbabi, A. Arbabi, A. Faraon, *Nanophotonics* **2018**, *7*, 1041.
- [3] F. Ding, Y. Yang, S. I. Bozhevolnyi, *Adv. Opt. Mater.* **2019**, *7*, 1801709.
- [4] P. Genevet, F. Capasso, F. Aieta, M. Khorasaninejad, R. Devlin, *Optica* **2017**, *4*, 139.
- [5] S. Jahani, Z. Jacob, *Nat. Nanotechnol.* **2016**, *11*, 23.
- [6] A. Zhan, S. Colburn, R. Trivedi, T. K. Fryett, C. M. Dodson, A. Majumdar, *ACS Photonics* **2016**, *3*, 209.
- [7] Q. Jiang, G. Jin, L. Cao, *Adv. Opt. Photonics* **2019**, *11*, 518.
- [8] A. Chizari, S. Abdollahramezani, M. V. Jamali, J. A. Salehi, *Opt. Lett.* **2016**, *41*, 3451.
- [9] Y. Shen, N. C. Harris, S. Skirlo, M. Prabhu, T. Baehr-Jones, M. Hochberg, X. Sun, S. Zhao, H. Larochelle, D. Englund, M. Soljačić, *Nat. Photonics* **2017**, *11*, 441.
- [10] T. Zhu, Y. Zhou, Y. Lou, H. Ye, M. Qiu, Z. Ruan, S. Fan, *Nat. Commun.* **2017**, *8*, 15391.
- [11] S. Abdollahramezani, A. Chizari, A. E. Dorche, M. V. Jamali, J. A. Salehi, *Opt. Lett.* **2017**, *42*, 1197.
- [12] S. Colburn, A. Zhan, A. Majumdar, *Sci. Adv.* **2018**, *4*, eaar2114.
- [13] X. Liu, T. Tyler, T. Starr, A. F. Starr, N. M. Jokerst, W. J. Padilla, *Phys. Rev. Lett.* **2011**, *107*, 045901.
- [14] F. Ding, Y. Jin, B. Li, H. Cheng, L. Mo, S. He, *Laser Photonics Rev.* **2014**, *8*, 946.
- [15] W. Wu, J. B. Dunlop, S. J. Collocott, B. A. Kalan, *IEEE Trans. Magn.* **2003**, *39*, 3334.
- [16] J. A. Bossard, L. Lin, S. Yun, L. Liu, D. H. Werner, T. S. Mayer, *ACS Nano* **2014**, *8*, 1517.
- [17] M. Mansouree, A. Arbabi, *CLEO: QELS Fundamental Science, FF1F–7*, Optical Society of America, Washington D.C. **2018**.
- [18] M. Mansouree, A. Arbabi, International Applied Computational Electromagnetics Society Symposium (ACES), IEEE, Miami, FL **2019**, pp. 1–2.
- [19] J. Jiang, J. A. Fan, arXiv preprint arXiv:1906.04157, **2019**.
- [20] Y. Kiarashinejad, S. Abdollahramezani, A. Adibi, arXiv preprint arXiv:1902.03865, **2019**.
- [21] K. Yao, R. Unni, Y. Zheng, *Nanophotonics* **2019**, *8*, 339.
- [22] M. H. Tahersima, K. Kojima, T. Koike-Akino, D. Jha, B. Wang, C. Lin, K. Parsons, *Sci. Rep.* **2019**, *9*, 1368.
- [23] W. Ma, F. Cheng, Y. Liu, *ACS Nano* **2018**, *12*, 6326.
- [24] S. D. Campbell, D. Sell, R. P. Jenkins, E. B. Whiting, J. A. Fan, D. H. Werner, *Opt. Mater. Express* **2019**, *9*, 1842.
- [25] I. Sajedian, T. Badloe, J. Rho, *Opt. Express* **2019**, *27*, 5874.
- [26] J. Baxter, A. C. Lesina, J.-M. Guay, A. Weck, P. Berini, L. Ramunno, arXiv preprint arXiv:1902.05898, **2019**.
- [27] Y. Long, J. Ren, Y. Li, H. Chen, *Appl. Phys. Lett.* **2019**, *114*, 181105.
- [28] S. An, B. Zheng, H. Tang, M. Y. Shalaginov, L. Zhou, H. Li, T. Gu, J. Hu, C. Fowler, H. Zhang, arXiv preprint arXiv:1908.04851, **2019**.
- [29] Z. A. Kudyshev, S. Bogdanov, T. Isacsson, A. V. Kildishev, A. Boltasseva, V. M. Shalae, arXiv preprint arXiv:1908.08577, **2019**.
- [30] Z. Liu, D. Zhu, S. P. Rodrigues, K.-T. Lee, W. Cai, *Nano Lett.* **2018**, *18*, 6570.
- [31] T. Qiu, X. Shi, J. Wang, Y. Li, S. Qu, Q. Cheng, T. Cui, S. Sui, *Adv. Sci.* **2019**, *6*, 1900128.
- [32] R. S. Hegde, *IEEE J. Sel. Top. Quantum Electron.* **2019**, *26*, 1.
- [33] R. S. Hegde, *Opt. Eng.* **2019**, *58*, 065103.
- [34] L. Gao, X. Li, D. Liu, L. Wang, Z. Yu, *Adv. Mater.* **2019**, *31*, 1905467.
- [35] C. C. Nadell, B. Huang, J. M. Malof, W. J. Padilla, *Opt. Express* **2019**, *27*, 27523.
- [36] D. Melati, Y. Grinberg, M. K. Dezfouli, S. Janz, P. Cheben, J. H. Schmid, A. Sánchez-Postigo, D.-X. Xu, *Nat. Commun.* **2019**, *10*, 1.
- [37] Y. Kiarashinejad, S. Abdollahramezani, M. Zandehshahvar, O. Hemmatyar, A. Adibi, *Adv. Theory Simul.* **2019**, *2*, 1900088.
- [38] O. Hemmatyar, S. Abdollahramezani, Y. Kiarashinejad, M. Zandehshahvar, A. Adibi, *Nanoscale* **2019**, *11*, 21266.
- [39] S. Boyd, L. Vandenberghe, *Convex Optimization*, Cambridge University Press, Cambridge **2004**.
- [40] M. Meilă, *J. Multivar. Anal.* **2007**, *98*, 873.
- [41] Y.-C. Chen, M. Meilă, arXiv preprint arXiv:1907.01651, **2019**.
- [42] D. Perraul-Joncas, M. Meila, arXiv preprint arXiv:1305.7255, **2013**.
- [43] A. Patrikainen, M. Meila, *IEEE Trans. Knowl. Data Eng.* **2006**, *18*, 902.
- [44] S. Jin, R. Zafarani, IEEE International Conference on Data Mining (ICDM), IEEE, Singapore **2018**, pp. 177–186.
- [45] S. Jin, V. V. Phoha, R. Zafarani, IEEE International Conf. on Data Mining (ICDM) **2019**.
- [46] G. E. Hinton, R. R. Salakhutdinov, *Science* **2006**, *313*, 504.
- [47] C. B. Barber, D. P. Dobkin, D. P. Dobkin, H. Huhdanpaa, *ACM Trans. Math. Software* **1996**, *22*, 469.
- [48] B. Schölkopf, R. C. Williamson, A. J. Smola, J. Shawe-Taylor, J. C. Platt, *Advances in Neural Information Processing Systems*, MIT Press **2000**, pp. 582–588.
- [49] U. Fano, *Phys. Rev.* **1866**, *124*, 1961.
- [50] M. F. Limonov, M. V. Rybin, A. N. Poddubny, Y. S. Kivshar, *Nat. Photonics* **2017**, *11*, 543.
- [51] R. C. Devlin, M. Khorasaninejad, W. T. Chen, J. Oh, F. Capasso, *Proc. Natl. Acad. Sci.* **2016**, *113*, 10473.
- [52] E. D. Palik, *Handbook of Optical Constants of Solids*, Vol. 3. Academic Press, Washington D.C. **1998**.